Czech Technical University in Prague

Faculty of Electrical Engineering
Department of Cybernetics

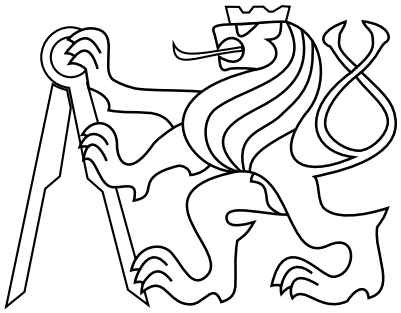

Ray Tracing Simulation of X-Ray optical Systems for Space Applications

Bachelor's Thesis

Daniel Malfatti

Prague, May 2023

Study programme: Cybernetics and Robotics

Thesis supervisor: Ing. Tomáš Bača, Ph.D.

BACHELOR'S THESIS ASSIGNMENT

I. Personal and study details

Student's name: **Malfatti Daniel** Personal ID number: **492325**

Faculty / Institute: **Faculty of Electrical Engineering**

Department / Institute: **Department of Cybernetics**

Study program: **Cybernetics and Robotics**

II. Bachelor's thesis details

Bachelor's thesis title in English:

Ray Tracing Simulation of X-Ray Optical Systems for Space Applications

Bachelor's thesis title in Czech:

Paprsková simulace X-Ray optických systémů pro kosmické mise

Guidelines:

The focusing optics of X-Ray telescopes differ significantly from the design for the visible-light spectrum. The focusing elements for X-Ray use reflective elements rather than lenses. The optics are typically a complex system composed of flat or curved mirrors that collectively focus the incoming parallel rays onto a sensitive detector. The development of X-Ray telescopes, such as those currently tested onboard VZLUSAT-1 [1] and VZLUSAT-2 satellites, is challenging without simulations. This thesis will focus on designing and developing software for ray tracing simulation of X-Ray optical systems of the Lobster-Eye design. Simulation should not only compute the expected results based on the parameters of the optics but also consider a potential direct line of sight along the surrounding mechanical fixtures and their 3D shape. The work will be divided into the following parts:
The student will familiarize himself with the field of high-energy photon physics, their focusing, and detection.
The student will research suitable tools for prototyping and implementation for X-Ray ray tracking simulation [2, 3].
The student will design and implement the software for simulating the output of Lobster-Eye optics.
The implemented software will be tested on examples of real-world systems, and the results will be compared with laboratory data obtained from available space missions.
The student will simulate the expected measured data from the available space missions (REX, VZLUSAT-1 [1, 2]).

Bibliography / sources:

[1] Baca, T., et al. "Miniaturized X-ray telescope for VZLUSAT-1 nanosatellite with Timepix detector." Journal of Instrumentation 11.10 (2016): C10007.
[2] Urban, M., Nentvich, O., Báča, T., Veřtát, I., Maršíková, V., Doubravová, D., ... & Tutt, J. H. (2021). REX: X-ray experiment on the water recovery rocket. Acta Astronautica, 184, 1-10.
[3] Davis, John E., et al. "Raytracing with MARX: X-ray observatory design, calibration, and support." Space Telescopes and Instrumentation 2012: Ultraviolet to Gamma Ray. Vol. 8443. SPIE, 2012.
[4] Tichý, Vladimír, René Hudec, and Šárka Němcová. "Effective algorithm for ray-tracing simulations of lobster eye and similar reflective optical systems." Experimental Astronomy 41.3 (2016): 377-392.

Name and workplace of bachelor's thesis supervisor:

Ing. Tomáš Báča, Ph.D. Multi-robot Systems FEE

Name and workplace of second bachelor's thesis supervisor or consultant:

Date of bachelor's thesis assignment: **18.01.2023** Deadline for bachelor thesis submission: **26.05.2023**

Assignment valid until: **22.09.2024**

Ing. Tomáš Báča, Ph.D.	prof. Ing. Tomáš Svoboda, Ph.D.	prof. Mgr. Petr Páta, Ph.D.
Supervisor's signature	Head of department's signature	Dean's signature

III. Assignment receipt

The student acknowledges that the bachelor's thesis is an individual work. The student must produce his thesis without the assistance of others, with the exception of provided consultations. Within the bachelor's thesis, the author must state the names of consultants and include a list of references.

. _____
Date of assignment receipt

_____
Student's signature

Author statement for undergraduate thesis:

I declare that the presented work was developed independently and that I have listed all sources of information used within it in accordance with the methodical instructions for observing the ethical principles in the preparation of university theses.

Prague, May 26, 2023 Daniel Malfatti

Acknowledgments

Firstly, I would like to express my gratitude to my thesis supervisor Dr. Tomáš Bača, for his guidance, patience and support throughout the entire research process. His willingness to share his knowledge and experience has made this not only an educative but also an enjoyable experience. My deepest appreciation goes to my family and particularly my sister, who has been a huge support throughout this whole process.

Abstract

This thesis deals with the challenges associated with developing optics for space telescopes capable of focusing high-energy photons, namely focusing on lobster-eye optics. The main objective of this thesis is to explore the unique properties of lobster-eye optics and develop a simulator to model their behavior. To evaluate the implementation of the simulator, the simulator is tested using scenarios inspired by real-life missions VZLUSAT-1 and Rocket Experiment (REX). These tests aim to uncover the potential hurdles that may have hindered these missions and illustrate the capabilities of the simulator. The final result of this thesis should contribute to the future development of lobster-eye optics by providing a versatile, user-friendly tool that could serve in the development phase by uncovering any design flaws and aiding in interpreting the data post-deployment.

Keywords: high-energy photons, lobster-eye optics, ray-tracing simulator, telescope design, VZLUSAT-1, REX mission

Abstrakt

Tato práce se zabývá výzvami spojenými s vývojem optiky pro vesmírné teleskopy schopné zaměřovat vysokoenergetické fotony, přičemž se zaměřuje zejména na tzv. optiku typu račí oko. Hlavním cílem této práce je prozkoumat unikátní vlastnosti optiky typu račí oko a vyvinout simulátor pro modelování jejího chování. Pro ověření implementace simulátoru jsou použity scénáře inspirované reálnými misemi VZLUSAT-1 a REX. Tyto testy si kladou za cíl odhalit případné překážky, které mohly nastat v těchto misích, a ilustrovat schopnosti simulátoru. Výsledkem této práce by mělo být přispění k budoucímu rozvoji optiky typu račí oko poskytnutím všestranného a uživatelsky přívětivého nástroje, který by mohl sloužit jak ve fázi vývoje, odhalení případných konstrukčních nedostatků, tak k interpretaci dat po nasazení.

Klíčová slova: vysokoenergetické fotony, optika typu račí oko, simulátor paprsků, návrh dalekohledu, mise VZLUSAT-1, mise REX

Contents

List of Figures

List of Tables

Abbreviations

API Application Programming Interface

CERN European Council for Nuclear Research

LEO Low Earth Orbit

MFO Multi Foil Optics

FOV Field of View

REX Rocket Experiment

WRX-R Water Recovery X-ray Rocket

PSU Pennsylvania State University

IMU Inertial Measurement Unit

NASA The National Aeronautics and Space Administration

SNR Supernova Remnant

HXMT Hard X-ray Modulation Telescope

MARXS Multi-Architecture X-ray Simulator

CTU Czech Technical University in Prague

STL Standard Triangle Language

CAD Computer Aided Design

IR Infrared Radiation

Chapter 1

Introduction

1.1 Background and Motivation

With our current understanding of physics, the most efficient way to study the universe is by observing the ample spectrum of electromagnetic radiation with which all bodies of matter known to us interact.

Doing so is crucial in understanding the development of the universe and the driving forces behind it. Different aspects of the cosmos reveal themselves through different parts of the electromagnetic spectrum. For example, due to the universe's expansion, low-energy electromagnetic waves can give us insight into far-off galaxies and events [29]. At the same time, phenomena such as the birth or death of stars can reveal themselves through a burst of high-energy electromagnetic waves [18].

Observing such phenomena is also a great way of testing the accuracy of our theoretical model of the universe. In the last few decades, there have been substantial advancements to our model of the universe, thanks to the many innovations in the field of astronomy. For example, the reintroduction of the cosmological constant thanks to the observation of the acceleration of the universe's expansion [30] or, consequently, the discovery of dark energy [26] that have recently spurred attempts to derive a correlation between them and vacuum energy contained in black holes [1].

Observing celestial bodies with the naked eye or using glass optics-based telescopes is no novelty. It has been available for centuries; however, observing space from within the Earth's atmosphere poses many constraints, mainly that a large part of the electromagnetic spectrum is filtered by the Earth's atmosphere.

Some of the most extreme and elusive phenomena in space emit high-energy photons [27]. To gather valuable information about these entities, we need to construct a telescope capable of capturing a sizeable portion of high-energy electromagnetic radiation from outside the Earth's atmosphere and communicating it back to Earth.

1.2 Research objectives

The primary objective of this thesis is to introduce the challenges associated with focusing and detecting high-energy photons, particularly in the case of lobster-eye optics used in space telescopes. The aim is to explore lobster-eye optics' unique properties and advantages to solve these challenges.

Furthermore, a key goal of this thesis is to develop a simple ray-tracing simulator capable of accurately modeling the trajectories of X-ray photons in a lobster-eye telescope. The

simulator will serve as a valuable tool for evaluating the efficiency and performance of different lobster-eye optic designs.

The simulator will be applied to analyze and test the telescopes used in the VZLUSAT-1 and REX missions. By subjecting the telescope simulation to unique scenarios not considered during the design phase of the telescopes and comparing the simulation results with data gathered during these missions, the analysis will provide a possible explanation for the anomalies observed during the missions.

Through these research objectives, this thesis aims to provide a flexible, user-friendly tool to facilitate the development of lobster-eye telescopes and gain insights into operational behavior and performance in real-world scenarios.

Chapter 2

Optical designs for high-energy photon focusing

While launching a telescope outside the Earth's atmosphere and maintaining functionality in a harsh environment is in itself a challenge, the main challenge, and the one this thesis will be focusing on, is the design of optics capable of efficiently focusing high-energy photons for space missions.

2.1 Brief overview of Photon-Matter Interactions

To design an optical system that manipulates the trajectories of photons, it is first important to understand the primary interaction mechanisms between photons and matter. To fully comprehend these interactions, it is first necessary to be familiar with the intricacies of quantum electrodynamics, and since that would exceed the scope of this work, I will limit the description only to a brief overview. While many factors influence the probabilities of these interactions, the ones relevant to this work are the photon's energy, the angle of incidence, and the atomic properties of the material. In the field of high-energy photon physics, there are four main interactions.

2.1.1 The Photoelectric Effect

Firstly, the photoelectric effect [36] describes the total absorption of a photon by matter. When a photon with certain energy hits a surface, it is absorbed, and its energy is transferred to an electron, causing it to be ejected from the surface. For high-energy photons, the probability of absorption is significantly high, posing a challenge for the design of optics.

2.1.2 Compton Scattering

Secondly, Compton scattering [37] describes the change in a photon's direction and wavelength upon interaction with matter. When a photon collides with an electron, it imparts some of its energy, altering its wavelength and direction. Compton scattering is the dominant interaction mechanism for photons in the X-ray energy range.

2.1.3 Pair Production

The third interaction, pair production [32], describes the creation of an electron-positron pair from a photon's energy when it comes into proximity with the nucleus of an atom. This

interaction is usually prevalent for extremely high-energy photons, which are not discussed in this work, and thus can be omitted in our case.

2.1.4 Rayleigh Scattering

The fourth and final interaction is Rayleigh scattering [38], which describes the scattering of photons by particles much smaller than the wavelength of the light. When a photon hits a molecule, it imparts its energy, causing the molecule to vibrate and, in turn, emit a photon with the same energy but in a different direction. This interaction is more prevalent in lower-energy photon ranges. However, it can occur with X-rays by adjusting the incidence angle and choosing a material with appropriate atomic properties.

2.2 Principles of optics types and challenges

The most commonly used types of optics are pinhole optics, mirror optics, and lenses.

2.2.1 Pinhole optics

Pinhole optics [19] allow photons to pass through a narrow hole until they hit a detector, forming an inverted image of the observed object. The principle is illustrated in figure 2.1. While pinhole optics are easy to construct and have few constraints on the choice of material to construct them, due to their small aperture size, their efficiency greatly depends on the source's intensity. Simple pinhole optics would, therefore, not be suited for observing faint, far-away sources of electromagnetic radiation.

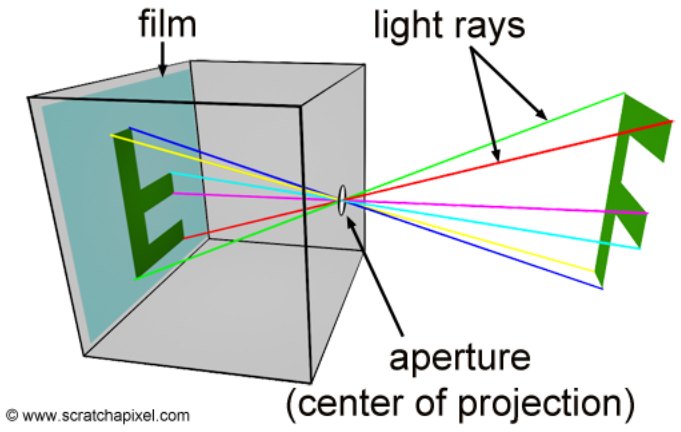

Figure 2.1: Illustration of the principle of a basic pinhole optical system. The rays emitted by the source object, in this case, a letter, pass through a narrow opening to create an inverted image. Courtesy of [39].

2.2.2 Mirror optics

Mirror optics reflect photons using a set of mirrors until they hit a detector to form an image. The principle is illustrated in figure 2.2. The reflection of X-ray photons, however, is a

complex matter due to their high energy and the way they tend to penetrate and scatter off of matter. Typical values of the critical angle of incidence below which reflection occurs for X-rays interacting with golden or iridium mirrors are below three degrees [8], which makes standard mirror optics configurations used in space telescopes, for example, the one used recently in the James Webb telescope [15], not suited for X-ray detection purposes.

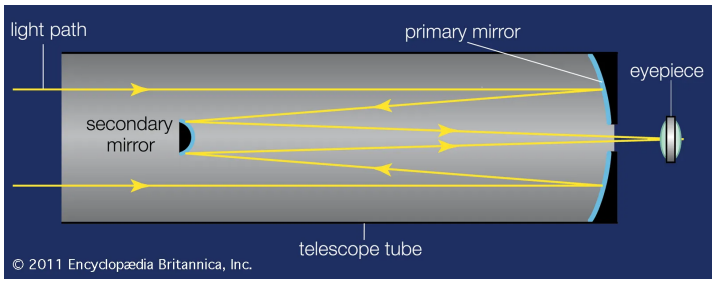

Figure 2.2: Illustration of the lightpath of a cessegrain optical mirror system. The rays pass through the aperture and are reflected by a primary and a secondary mirror until they hit a detector. For this design, the mirrors need to be able to reflect rays at steep angles. Courtesy of [12].

2.2.3 Lenses

Lenses allow photons to pass through material which alters their trajectory in a way that they hit the detector and form an image. The principle is illustrated in figure 2.3. Similarly to mirror optics, lenses suffer from constraints where finding a material that is able to alter the trajectory of a high-energy photon is very challenging. While there have been attempts at focusing X-rays through refraction [24], the solutions have not been widely adopted due to the construction's complexity and inability to function properly in outer space's harsh and unpredictable environment.

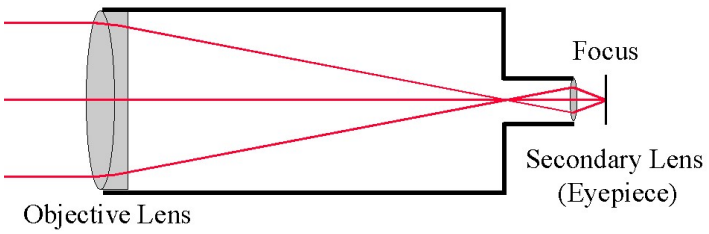

Figure 2.3: Illustration of the principle of a lens optical system. The trajectory of the rays is altered as they pass through the lens. Courtesy of [22].

2.3 Lobster-eye optics

As often happens with problems in engineering, a possible solution can be found in nature. So-called lobster-eye optics, which get their name from and mimic the structure of the eyes of crustaceans, use a combination of the principles of pinhole and mirror optics. The structure of the optics can be seen in figure 2.4.

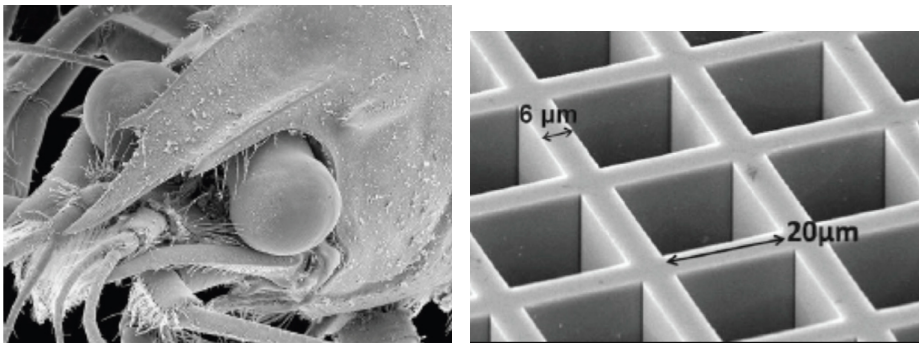

(a) The eye of a lobster. (b) Close view of the microchannels.

Figure 2.4: A close view of a lobster's eye, which is comprised of tiny reflective square-shaped microchannels 2.4a. Additionally, a closer view of how the microchannels are arranged in a lobster-eye optic 2.4b. Courtesy of [6].

Unlike the basic pinhole optics, lobster-eye optics are comprised of tiny reflective square-shaped microchannels arranged in a spherical configuration. The microchannels are angled to reflect the radiation toward the detector. The reflection occurs at a shallow angle, allowing the photons to penetrate deeper into the channels before being reflected. This design enables lobster-eye optics to not only let direct rays through but also focus rays through grazing incidence reflections along their path to the detector, usually placed at a distance equal to half the radius of the configuration sphere from the center of the configuration sphere.

The first design was proposed in 1979 by Angel [33], with the initial aim to create an X-ray telescope with a Field of View (FOV) as large as possible. Since then, many variations, such as the Schmidt arrangement [35], have been developed to simplify the construction process and achieve similar results. An illustration of some designs can be seen in figure 2.5. Although there are other designs available, this work will focus solely on the Schmidt arrangement, as it is the configuration used by the missions being discussed.

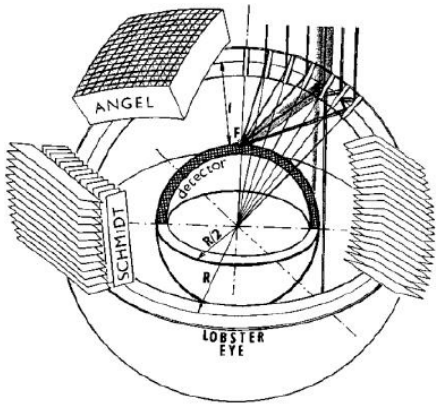

Figure 2.5: Illustration of the different designs of lobster-eye optics arranged on a sphere to illustrate the ideal arrangement of these optics together with a spherical detector. Courtesy of [20].

2.4 Detection

The most commonly used X-ray detectors work on similar principles as other semiconductor optical detectors. However, as was touched upon in the previous section, high-energy photons interact with matter in a more complex way than the rest of the electromagnetic spectrum; consequently, the issue of detection suffers from similar problems, and a multitude of approaches exist. However, the main focus of this work is to study the photon's trajectory from the optics to the detector, so the efficiency with which the detector is able to capture them can be altered at the end of the simulation accordingly to the characteristics of the detector used.

The detector used in the missions discussed in this work is the Timepix detector [21], developed at European Council for Nuclear Research (CERN). The Timepix detector combines a semiconductor sensor with a pixel readout chip, providing high spatial and energy resolution. The structure of the detector is illustrated in figure 2.6. The way the detector operates is by detecting the electric charge generated by the penetrating ionizing particle in the detector, which is then collected in a discrete rectangular grid of pixels, and the signal is further processed. Data from the sensor can be read out at a rate of up to 100 images per second.

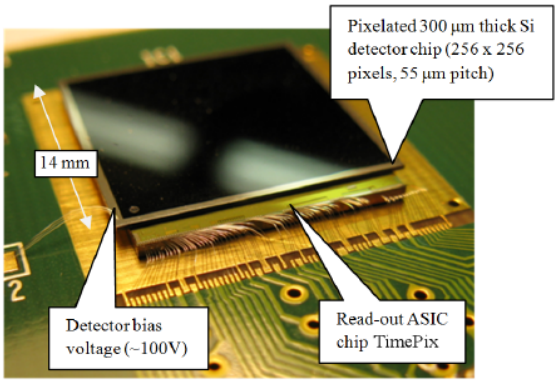

Figure 2.6: A close view of the Timepix detector, its dimensions, and main components. Courtesy of [14].

Chapter 3

Missions

This chapter will give a brief overview of the missions on which the developed simulator was tested, focusing mainly on the aspects relevant to this work.

3.1 VZLUSAT-1

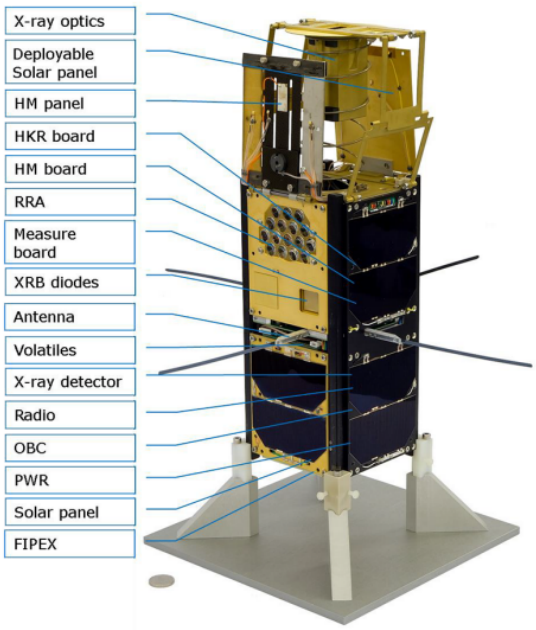

Figure 3.1: An outside view of the VZLUSAT-1 satellite with its components highlighted. Courtesy of [9].

The first telescope discussed in this work is the VZLUSAT-1 X-ray telescope [9], launched into sun-synchronous Low Earth Orbit (LEO) as part of the QB50 mission [3], whose primary aim was to observe Earth's lower thermosphere during atmospheric descent. The outside structure of the telescope can be seen in figure 3.1. The X-ray telescope utilizes the first-ever lobster-eye Multi Foil Optics (MFO) Schmidt X-ray optics in space. While its main objective is to test the efficiency of this design in space, it should also provide valuable information by observing the X-ray radiation of celestial bodies.

3.1.1 VZLUSAT-1 X-ray telescope structure

The telescope comprises two main parts: a one-dimensional Schmidt-type lobster-eye optical module with a wide FOV and a silicon-based hybrid semiconductor detector, Timepix. The internal view of the telescope can be seen in figure 3.2.

The optical module consists of 56 double-sided gold-coated glass foils arranged accordingly to achieve a FOV of up to three degrees and to give an idea of the observed object's position in the second dimension; a non-reflective tungsten bar is placed orthogonally to the foils, as seen in figure 3.3 in front of them to produce a shadow in the final image.

The sensor is placed at a distance of a focal length of 250 mm from the optic module. The Timepix sensor used holds the shape of a $14 \times 14\,\mathrm{mm}^2$ with a resolution of 256×256 evenly-sized pixels.

The arrangement should be able to capture X-rays in the range of 5 to 20 keV. A notable design choice is the absence of radiation shielding in the direction of the optics, which is a novelty in the design of such telescopes. This decision implies that suitable data filtering of the final image will be needed if at all possible.

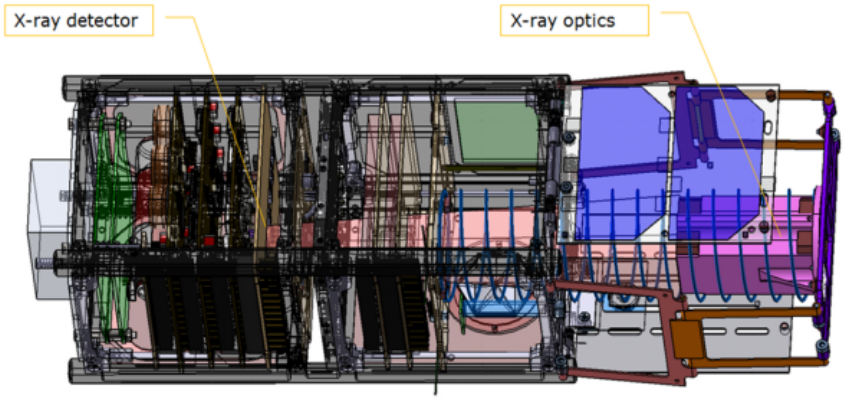

Figure 3.2: An inside view of the VZLUSAT-1 sattelite's 3D model. The optics module's position and the position of the detector can be seen as highlighted. Courtesy of [11].

3.1.2 The Sun as a source of X-ray radiation

While the Sun's light spectrum, when modeled by Planck's law of blackbody radiation, might suggest it is a weak source of X-ray radiation, the opposite is actually true. The Sun produces X-rays mainly during high-energy eruptions in its atmosphere, commonly known as solar flares [17]. For an observer positioned closely outside the Earth's atmosphere, the Sun is the most prominent source of X-rays. This phenomenon makes the Sun a prime candidate for both testing the design of the aforementioned X-ray telescope and for data gathering, as it could possibly shine some light on the highly volatile behavior of the Sun's atmosphere.

The satellite was launched on July 23, 2017 and while being designed to operate for two years has been operational for six years and has captured a vast amount of data discussed in later chapters.

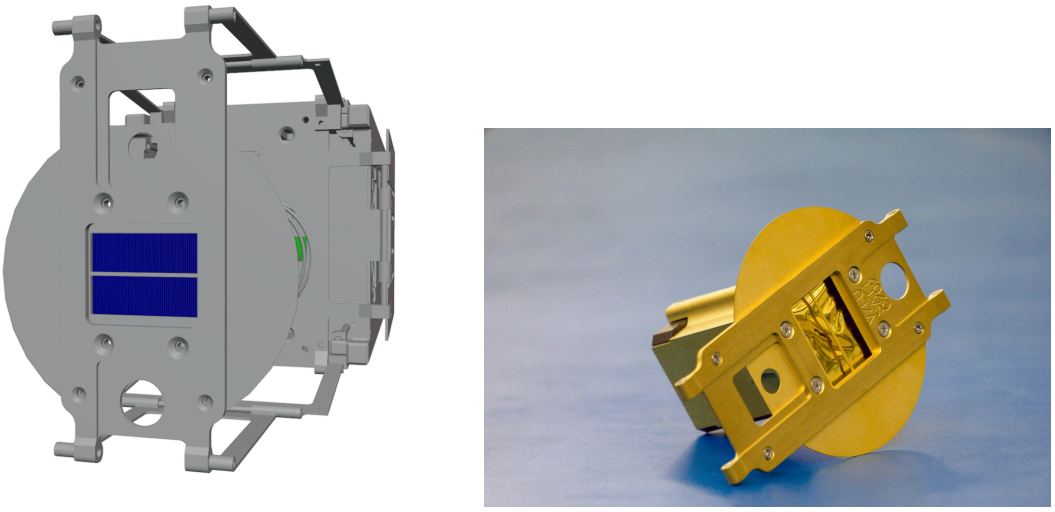

(a) Model view of the telescope.

(b) Real view of optics module.

Figure 3.3: Model view of the VZLUSAT-1 telescope with the tungsten bar (colored grey) orthogonal to optic foils (colored blue) and the detector (colored green) in the simulation setup done in Blender 3.3a. A photo of the optics module taken during assembly 3.3b, courtesy of [11].

3.2 REX1

The second telescope discussed is the REX telescope [2], launched as part of the WRX-R experiment [5] led by the Pennsylvania State University (PSU). REX was a secondary payload developed by a team of Czech scientists with the purpose of improving the design tested in the VZLUSAT-1 mission and testing the viability of its use in sounding rocket experiments. The arrangement of the payloads can be seen in figure 3.4.

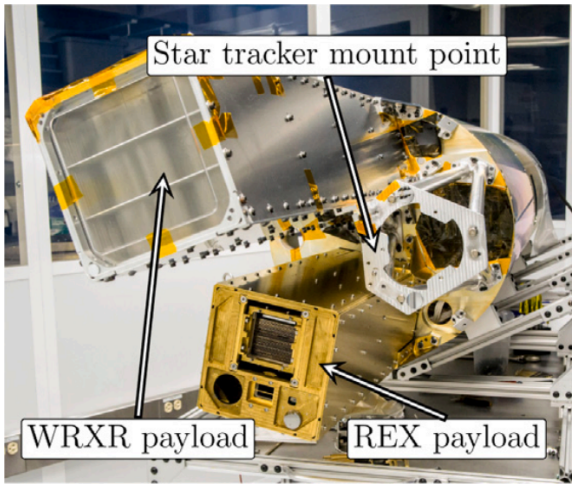

Figure 3.4: A picture taken during assembly of the payloads of WRX-R. The individual payloads are highlighted. Courtesy of [2].

Sounding rockets, unlike orbital satellites, are designed to last in space for a relatively short period of time, typically ranging from a few to tens of minutes, before they fall back to

Earth. This means they do not need to reach orbital speed and only need to survive the harsh environment of space for a limited amount of time. This makes the construction of sounding rockets generally cheaper and faster. Sounding rockets can also be precisely targeted to specific regions of interest, providing a high degree of precision when observing astrophysical bodies. However, the exposure time is limited by the time window the rocket allows before it falls back to Earth. These properties make sounding rockets ideal for missions with the goal of testing technologies in space, like the X-ray telescope, as long as the source's radiation is prominent enough. A picture of the rocket carrying the REX telescope can be seen in figure 3.5.

Figure 3.5: A picture of the sounding rocket carrying the REX telescope taken before launch. Courtesy of [2].

3.2.1 REX X-ray telescope structure

The REX payload is comprised of two independent X-ray lobster-eye telescopes. The primary telescope is composed of two X-ray lobster-eye MFO modules. These modules are orthogonal to one another, and each contains 47 double-sided gold-coated glass foils in the Schmidt arrangement. The modules are set up in series, creating a 2D system covering a FOV of 1×1.22 degrees. The primary telescope also includes a Timepix sensor identical to the one used in the VZLUSAT-1 mission located at a distance of 1420 mm from the front module to achieve a spectral range of 3 to 60 keV.

The secondary telescope is composed of a 1D lobster-eye MFO module and a Timepix sensor, set up the same way as in the VZLUSAT-1 mission.

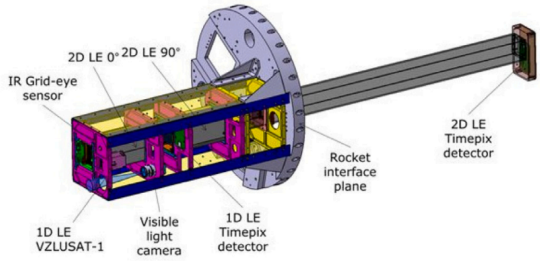

(a) Isometric view of the REX telescope's structure.

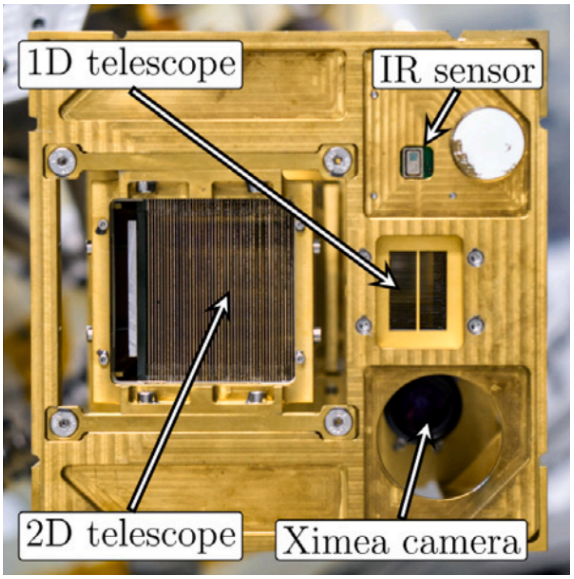

(b) Frontal view of the REX telescope.

Figure 3.6: An internal view of the REX telescope's 3D model with components highlighted 3.6a. A frontal view photo of the REX telescope taken during assembly with components highlighted 3.6b. Courtesy of [2].

Additionally, the payload was equipped with a Ximea camera to observe the visible light spectrum, an Infrared Radiation (IR) sensor array, and an Inertial Measurement Unit (IMU) to provide further information on the state and of the environment the rocket is in. The structure of the telesope can be seen in figure 3.6.

Unlike the structure of the VZLUSAT-1 telescope, REX provides radiation shielding in the direction of the optics, resulting in more precise data discussed in later chapters.

3.2.2 The Vela Supernova Remnant as a source of X-ray radiation

The observed astrophysical subject in this mission was the Vela Supernova Remnant (SNR), a remnant of a supernova explosion that occurred approximately 11400 years ago, approximately 250 pc away from Earth [28]. The structure of the Vela SNR revolves around a pulsar with a diameter of approximately 20 km according to The National Aeronautics and Space Administration (NASA) [7]. According to research done by the University of Birmingham [31], the pulsar should emit around 50 percent of the supernova remnant's overall radiation, making it the most prominent X-ray source and the observation's main focus.

Unlike the Sun, which has a more complex and less well-understood radiation spectrum, the Vela SNR has been extensively studied by other researchers, and its radiation spectrum is reasonably well characterized [31]. This makes the results of this mission easily verifiable.

.

Chapter 4

Development of Ray-Tracing Simulator

4.1 State of the art

A suitable tool for simulating the behavior of lobster-eye optics is crucial in the process of developing a lobster-eye telescope. Although the use of lobster-eye telescopes and their simulation is a relatively new and niche field, there are some simulation tools and software that researchers may adapt for their purposes.

One such example is GEANT4 [25], a toolkit developed at CERN for simulating the passage of particles through matter using Monte Carlo methods. The software was designed with modularity and flexibility, allowing it to be used in many different fields, including high-energy photon physics. An extension enabling the package to be used for X-ray tracing purposes specifically was developed by Buis and Vacanti [16] and has been used in the process of developing The Hard X-ray Modulation Telescope (HXMT) [10].

Another tool is the Multi-Architecture X-ray Simulator (MARXS) [4] developed at the Harvard-Smithsonian Center for Astrophysics. While MARXS is a general-purpose X-ray simulator not specifically designed for lobster-eye telescopes, its flexibility and capabilities make it a potentially useful tool for such simulations. It has been used in the development and analysis of several X-ray astronomy missions, such as ARCUS. Unlike the GEANT4 toolkit, it does not provide the ability to simulate the interaction of photons with matter in detail; however, it does provide a list of factors, such as reflection probabilities or grating efficiencies that the ray tracing takes into account, which can be beneficial mainly for performance issues.

Lastly, the Effective Algorithm for Ray Tracing Simulations of Lobster-Eye and Similar Reflective Optical Systems [13], developed at the Czech Technical University in Prague (CTU), merits mentioning. Although the software can be used to simulate other optical systems, it was developed with the specifics of the lobster-eye systems used in the missions discussed in this work in mind. Unlike the previous designs, the approach of this software was to create an accurate image of the output while casting as few rays as possible. This efficiency was possible by employing techniques similar to shadow casting commonly used in the field of computer graphics [34], although much simpler.

4.2 Mission statement

This thesis presents a simple X-ray ray tracing simulator designed to be used by anyone with a fundamental understanding of linear algebra and Python programming. The simulator has been crafted not only to evaluate the efficiency of lobster-eye optic designs but also to

test their operational behavior within the broader structure of a telescope. It can be used to identify potential design flaws, such as shadowing or shielding errors, that might arise within this complex system.

The simulator offers the flexibility to model rays from any source, provided it can be parameterized. However, instead of diving deep into the complex behaviors of light interacting with various materials, the simulator relies on a set of parameters influencing the ray tracing path, thus simplifying the process.

The simulator was developed with the intention of testing the results of the VZLUSAT-1 and REX missions. However, in principle, with a dash of ingenuity, it can be used for other similar purposes.

4.3 Problem analysis

The problem of simulating the behavior of X-ray photons in a lobster-eye optical system-based telescope is very similar to ray tracing problems. Ray tracing is a technique commonly used in the field of computer graphics to simulate the behavior of visible light to illuminate a scene. However, since high-energy photons interact with matter much differently than standard visible light, only a fraction of the tools most existing ray tracing algorithms provide is needed. Omitting gravitational lensing, which usually tends to curve the trajectory of photons and assuming the origin is far enough from the telescope, the trajectories of the photons can be modeled by a straight line in 3D space with an origin point $\mathbf{O}$ and a direction vector $\mathbf{d}$.

The coordinates of any point $\mathbf{p}$ on the trajectory can be expressed by the ray equation

$$\mathbf{p} = \mathbf{O} + t\mathbf{d}, \tag{4.1}$$

where $t \in \mathbb{R}$ and $t \geq 0$ since we assume the photons only move away from the origin in one direction.

As previously mentioned in section 2.3 of chapter 1, most lobster-eye lenses are composed of flat mirrors capable of reflecting a ray up to a certain critical angle of incidence. In this work, the focus will mainly be on the optical systems used in the VZLUSAT-1 and REX missions, which use the Schmidt arrangement where either one set of mirrors focuses rays in one direction only or two orthogonal sets of mirrors focus rays in both directions, as seen in figure 4.1 to produce a 2D image of the observed source of X-ray photons.

Considering that the flat mirror telescope optics are the only part of the telescope capable of reflection of X-rays and the rest simply absorbs the rays, the model of the telescope can be approximated by a discrete set of triangles in 3D space where the triangles approximating the surface of the optics mirrors are the only ones capable of reflection. In contrast, the remaining triangles merely absorb them. Such a triangle set can be easily obtained, for example, by converting the 3D model of the telescope into an Standard Triangle Language (STL) file, which most commonly available Computer Aided Design (CAD) software can produce.

4.4 Required Geometry

When tracing the trajectory of photons in a lobster-eye optical system telescope approximated by a triangle mesh, the first thing that needs to be determined is whether a ray and

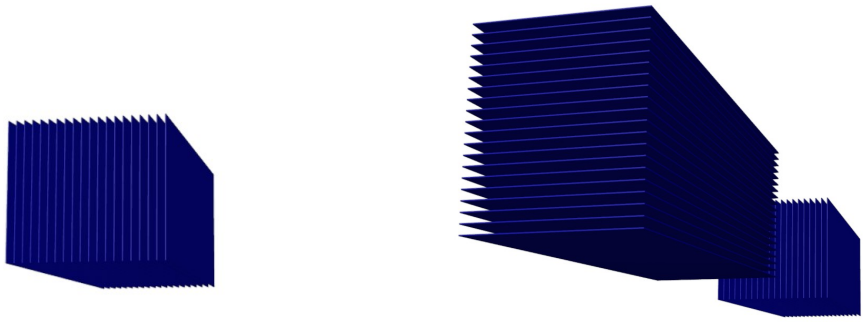

(a) One dimensional mirror system (b) Two dimensional mirror system

Figure 4.1: A model view of the 1D 4.1a and 2D 4.1b mirror systems respectively done in Blender. In both cases, the number of mirrors is reduced for clarity reasons.

a given triangle from the mesh intersect. An effective way to determine that is by using the Möller–Trumbore intersection algorithm [23], which takes advantage of the fact that all points within a triangle defined by three vertices $\mathbf{v_1}, \mathbf{v_2}, \mathbf{v_3}$ form a convex set since any line formed between them lies within the triangle and therefore any point $\mathbf{p}$ that lies in the triangle can be expressed as a convex combination of the tree vertices that define the triangle

$$\mathbf{p} = u\mathbf{v_1} + v\mathbf{v_2} + w\mathbf{v_3}, \tag{4.2}$$

where coefficients $u \in \mathbb{R}, v \in \mathbb{R}, w \in \mathbb{R}$ must, by definition of a convex combination, satisfy the following equation

$$u + v + w = 1, \tag{4.3}$$

$$u \geq 0, v \geq 0, w \geq 0. \tag{4.4}$$

The equation 4.2 can be rewritten by substituting for $w = 1 - u - v$ expressed from 4.3 as

$$\mathbf{p} = u\mathbf{v_1} + v\mathbf{v_2} + (1 - u - v)\mathbf{v_3}, \tag{4.5}$$

$$\mathbf{p} = u(\mathbf{v_1} - \mathbf{v_3}) + v(\mathbf{v_2} - \mathbf{v_3}) + \mathbf{v_3}. \tag{4.6}$$

Since the intersection point $\mathbf{p}$ must also satisfy the ray equation 4.1, the whole problem can be expressed as a system of linear equations

$$\begin{bmatrix}\mathbf{d} & (\mathbf{v_1} - \mathbf{v_3}) & (\mathbf{v_2} - \mathbf{v_3})\end{bmatrix} \begin{bmatrix} t \\ u \\ v \end{bmatrix} = \mathbf{O} - \mathbf{v_3}. \tag{4.7}$$

If the ray is not parallel to the triangle plane ($\mathbf{d}$ is not a linear combination of $(\mathbf{v_1} - \mathbf{v_3})$ and $(\mathbf{v_2} - \mathbf{v_3})$), the matrix must be regular and coefficients t, u, and v can be easily computed using Cramer's rule where

$$t = \frac{\det\begin{bmatrix}(\mathbf{O} - \mathbf{v_3}) & (\mathbf{v_1} - \mathbf{v_3}) & (\mathbf{v_2} - \mathbf{v_3})\end{bmatrix}}{\det\begin{bmatrix}\mathbf{d} & (\mathbf{v_1} - \mathbf{v_3}) & (\mathbf{v_2} - \mathbf{v_3})\end{bmatrix}}, \tag{4.8}$$

$$u = \frac{\det\begin{bmatrix}\mathbf{d} & (\mathbf{O}-\mathbf{v_3}) & (\mathbf{v_2}-\mathbf{v_3})\end{bmatrix}}{\det\begin{bmatrix}\mathbf{d} & (\mathbf{v_1}-\mathbf{v_3}) & (\mathbf{v_2}-\mathbf{v_3})\end{bmatrix}}, \tag{4.9}$$

$$v = \frac{\det\begin{bmatrix}\mathbf{d} & (\mathbf{v_1}-\mathbf{v_3}) & (\mathbf{O}-\mathbf{v_3})\end{bmatrix}}{\det\begin{bmatrix}\mathbf{d} & (\mathbf{v_1}-\mathbf{v_3}) & (\mathbf{v_2}-\mathbf{v_3})\end{bmatrix}}. \tag{4.10}$$

The point lies within the triangle if u and v are positive and sum to one.

Since the photons only pass in one direction, t must also be a positive non-zero number. If all these requirements are met, the intersection point coordinates can be easily computed from the ray equation 4.1.

Considering the physical properties of X-ray photons and the optics, a reflection off of the surface of the mirrors can happen only under a certain critical angle α.

Based on the configuration of the triangle normal $\mathbf{n}$ with respect to the direction of the ray $\mathbf{d}$ two instances can happen illustrated in figure 4.2a and figure 4.2b where the angle θ between $\mathbf{n}$ and $\mathbf{d}$ is either greater than 90° or less than 90°.

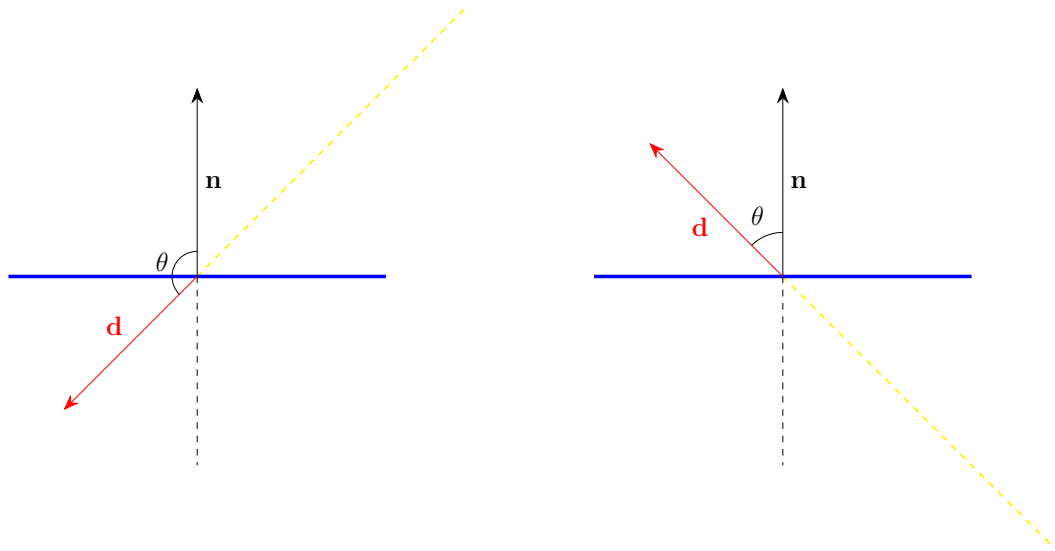

(a) Case where angle $\theta \geq \frac{\pi}{2}$.

(b) Case where angle $\theta \leq \frac{\pi}{2}$.

Figure 4.2: An illustration of the two distinct cases where the photons can hit a double-sided mirror. The surface of the mirror is illustrated by a thick blue line, the trajectory of the photons is illustrated by a dashed yellow line, the direction vector of the photons is colored red, and the normal vector of the surface is colored black. Case, where the angle θ between the surface normal $\mathbf{n}$ and the direction vector $\mathbf{d}$, is greater or equal to $\frac{\pi}{2}$ illustrated in figure 4.2a and case where θ is less than $\frac{\pi}{2}$ illustrated in figure 4.2b. Although the illustrations show the principle in two dimensions for clarity purposes, the same principle applies in three dimensions analogously.

Considering that the normal $\mathbf{n}$ is by definition perpendicular to the plane, the absolute value $|\frac{\pi}{2} - \theta|$ will always return a positive value equal to the incidence angle of the ray in both cases illustrated in figure 4.2a and figure 4.2b. The incidence angle can then be compared to the critical angle of incidence α to determine if a reflection is possible.

Once the intersection point of the ray and a given triangle is determined, the only remaining step is to reflect the ray. This process entails reflecting the direction vector of the ray given a surface normal. Using some basic vector algebra, it can be determined that the reflected vector $\mathbf{d_r}$ is equal to

$$\mathbf{d_r} = \mathbf{d} - 2(\mathbf{n} \cdot \mathbf{d})\mathbf{n}. \tag{4.11}$$

The relation 4.11 applies to both configurations as illustrated in figures 4.3a, 4.3b.

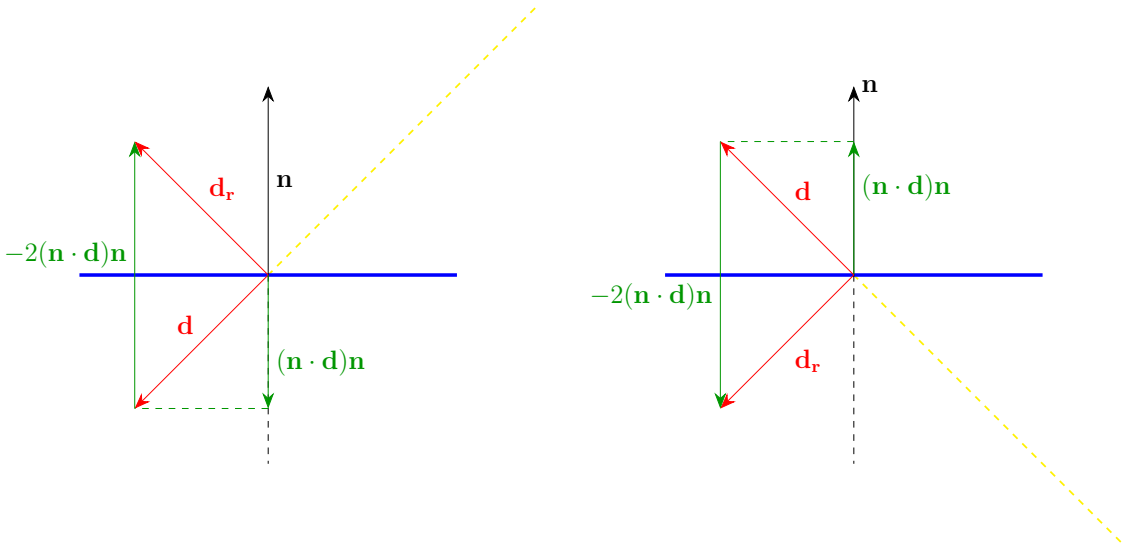

(a) Case of reflection where angle $\theta \geq \frac{\pi}{2}$.

(b) Case of reflection where angle $\theta \leq \frac{\pi}{2}$.

Figure 4.3: An illustration of possible instances of reflection. The surface is illustrated by a thick blue line, the trajectory of the photons is illustrated by a dashed yellow line, the direction vector of the photons is colored red, the normal vector of the surface is colored black, and additional helpful vectors are colored green. Case, where the angle θ between the surface normal $\mathbf{n}$ and the direction vector $\mathbf{d}$, is greater or equal to $\frac{\pi}{2}$ illustrated in 4.3a and case where θ is less than $\frac{\pi}{2}$ illustrated in 4.3b. Although the illustrations show the principle in two dimensions only for clarity purposes, the same principle applies in three dimensions analogously.

4.5 Ray tracing process

Given a 3D model of an X-ray telescope decomposed into a triangle mesh, with triangles belonging to the optic's mirrors being labeled as reflective as discussed in 4.3, tracing the trajectory of an X-ray photon from its origin to a sensor inside a telescope should follow these steps:

1. Find the ray triangle intersection for all the mesh triangles if there is one.
2. Find the nearest triangle the ray intersects.
3. Check if the nearest triangle belongs to the sensor.
   (a) If yes, save the ray and all previously saved reflected rays, if there are any, as the traced trajectory of the photon. Terminate the process for this ray.

   (b) If not, continue to the next step.
4. Check if the nearest intersecting triangle is reflective.
   (a) If it is not reflective, the photon has been absorbed. Terminate the process for this ray.
   (b) If it is reflective, continue to the next step.
5. Check if the incidence angle is less than the critical angle.
   (a) If it is not less than the critical angle, the ray has been absorbed. Terminate the process for this ray.
   (b) If it is less, continue to the next step.
6. Save the current ray as reflected and create a new ray with origin in the intersection and direction equal to the reflected direction over the triangle normal. Repeat the process with the reflected ray.

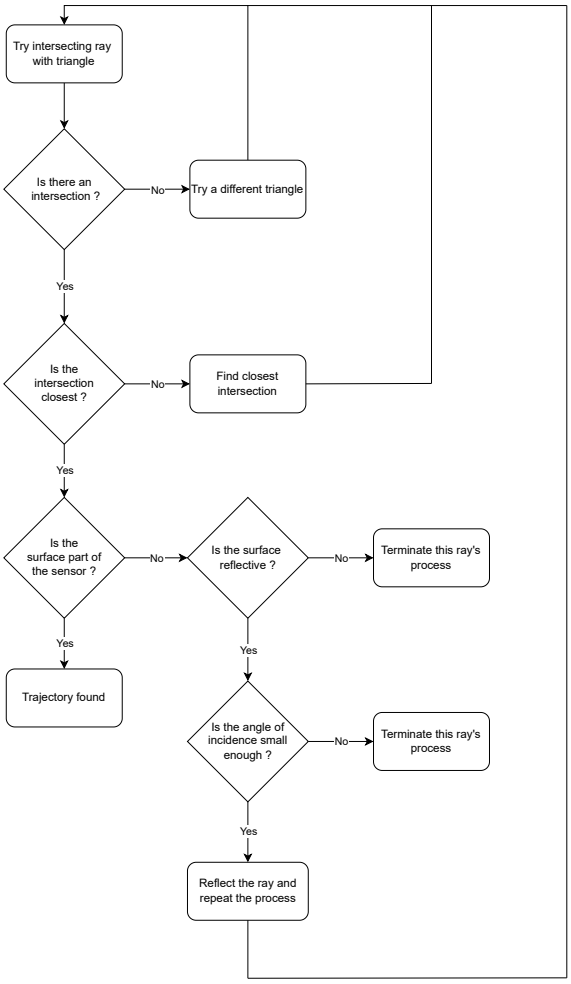

Figure 4.4: A flowchart of the ray tracing process as it was implemented in this work.

The flowchart of the process is illustrated in figure 4.4.

4.6 Performance optimizations

While in principle, the ray tracing process, as presented in the previous section, would produce correct results, considering all the possible directions the photons can travel from the origin and checking every triangle a telescope consists of for every iteration would be incredibly inefficient. For this reason, some simplifications regarding the telescopes examined in this work must be made.

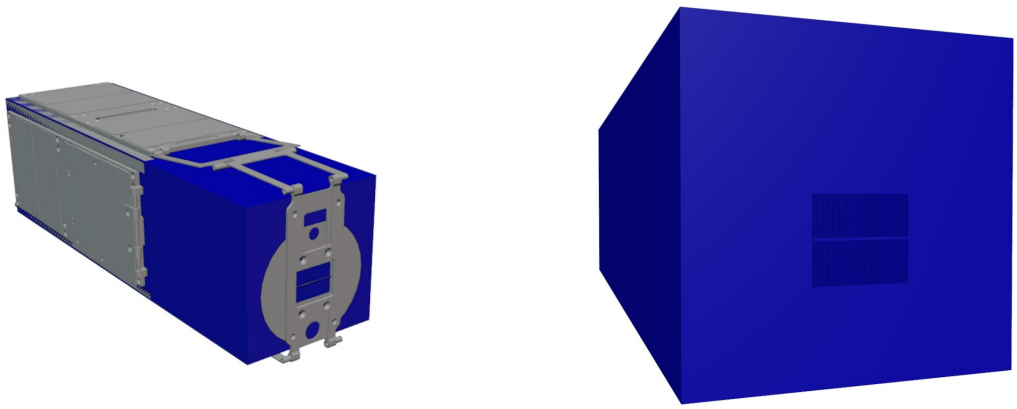

(a) Zoomed out model view of bounding box with the telescope's 3D model.

(b) Closer look at the bounding box with the optics and shielding bar.

Figure 4.5: Model image of one-dimensional lobster-eye optics telescope comprised of a rectangular bounding box with a hole for the optics aperture, the lobster-eye optics, and a shielding bar as was used in the VZLUSAT-1 mission. The model as it is used in the ideal case scenario is depicted in 4.5b, and the same model with the 3D model of the telescope's real structure superimposed on it can be seen in 4.5a.

First, regarding the target points of the rays in the simulations, we assume the rays pass from the source point only along the path of the optics to the detector. Therefore the relevant target points for these rays are evenly spaced within a rectangle that shares the same dimensions as the aperture of the optics. Importantly, this rectangle is coplanar to the detector, ensuring that we capture the behavior of the rays as they interact with the optics and subsequently reach the detector.

For ideal case scenarios, a rectangular box with a hole in the dimensions of the aperture of the optics located in the direction of the rays is created to shield the detector from any possible stray rays that could bypass the desired path to the detector. This arrangement can be seen in figure 4.5. This approximation is crucial in reducing the number of possible rays to only the ones relevant to understanding how efficient the optics are at focusing X-rays.

The bounding box and the flat rectangular optics can be decomposed into a much smaller amount of triangles to reduce the number of triangles to check every iteration to a minimum. In exact terms, the total number of triangles N_t needed for such a model can be determined as

$$N_t = 18 + 2 + 12 \cdot n_f, \tag{4.12}$$

where 18 is the number of triangles needed for the bounding box, 2 is the number of triangles

needed for the sensor, and n_f denotes the number of mirrors the optics comprise.

Since the simulation does not necessarily distinguish the different energy levels a photon can carry, the number of rays in a single simulation will be represented by the photon flux $\Phi = \frac{N}{A \cdot T}$, where N is the number of photons passing though area A in the time interval T. With our setup, N will be equal to the product of the number of source points and target points to satisfy the desired photon flux. If a distinction between photon energies is desired in the simulation, it can be simply achieved by running multiple different simulations with different sets of parameters to satisfy the behavior of the energy level of the photon, and the results can be later superimposed.

Depending on the structure of the source object, a discrete amount of point sources arranged to approximate the object's shape and the desired photon flux should suffice. The initial rays to be processed by the ray tracing process will then be defined to pass through both source and target points.

By doing these steps, the number of rays that need to be examined is significantly reduced.

While this simplification can be efficient in the case of simulating the trajectories of X-ray photons emitted from a high-intensity source, it does not reveal any flaws in the structure of the telescope itself. It can, however, be instrumental in revealing any structural flaws of the telescope that might obstruct rays passing from the optics to the sensor and cast shadows in the final image. This test can be done by simply gathering the rays that would pass in the ideal case and checking if they intersect with the telescope 3D model triangle mesh at any point along the trajectory.

Another convenient simplification when testing for structural flaws can be sorting the telescope's triangles based on their position in the direction of the rays. This approach takes advantage of the fact that the distances of the collision points between the rays and the telescope's triangles are not significant when searching for possible shadows cast on the detector. By sorting the triangles from closest to furthest from the source along the direction of the rays, the time complexity of the process can be significantly improved. This optimization allows for more efficient detection of potential structural flaws and reduces computational overhead in the simulation.

4.7 Visualization

When debugging or looking for structural flaws in the telescope, a simple yet efficient way to gain insight into the problem would be to visualize the situation that is trying to be simulated. This work utilized Blender, a powerful, open-source 3D computer graphics software tool, to model the simulation environment. Blender's Python Application Programming Interface (API) offers a vast amount of tools for 3D scene modeling. In the context of this simulator, the scene is comprised of several components. First, the 3D model of the telescope, its optics, and the detector are each modeled as separate objects. Next, the rays are represented as thin, elongated cylinders, further differentiated into two categories: direct rays and reflected rays. Finally, the collision points between rays and the telescope's structure can be modeled as small colored spheres. All these tools are provided by the bpy module within Blender, enabling the construction of an interactive, informative 3D model that greatly aids the debugging and development process.

.

Chapter 5

VZLUSAT-1 Mission Testing

The simulation of the X-ray telescope used in the VZLUSAT-1 mission focuses on two main cases: an ideal case scenario, which approximates the images obtained under optimal conditions, and a series of tests designed to possibly reveal the causes of some flawed data gathered during the mission.

5.1 Simulation setup

As discussed in previous chapters, the primary target of the X-ray telescope's observations was the Sun. Given the highly volatile nature of the Sun's radiation in the X-ray spectrum, the simulation will focus on finding a range of the photon flux necessary to obtain an image containing enough valuable information. This approach will allow us to understand the telescope's performance under optimal conditions and gain insights into the potential issues that could have led to anomalies in the observed data.

The distance of the Sun from LEO can fluctuate depending on the Earth's position in its orbit around the Sun. However, to simplify our simulations, we will consider only the average distance of 149.6×10^6 km. Similarly, the apparent dimensions of the Sun can also vary due to the elliptical nature of Earth's orbit. For the purpose of these simulations, we will use a consistent angular diameter of 0.5 degrees. To model the Sun as a source of radiation in our simulations, we will approximate it as a series of discrete point sources of radiation arranged into concentric circles on a disk facing the telescope, imitating the Sun's spherical shape and uniform radiation distribution. This approximation allows us to capture the broad, overall behavior of the telescope under solar observation without getting into the complexities of the Sun's detailed structure and radiation patterns. The parameters of the optics are summarized in 5.1.

Foil width	25.0 mm
Foil length	60.0 mm
Foil thickness	0.145 mm
Number of foils	56
Focal length	250.0 mm
FOV	3°
Aperture area	841 mm^2
Critical angle	0.25°

Table 5.1: Parameters of the 1D Schmidth type lobster-eye optics.

5.2 Ideal case scenario

In the first simulation, the Sun was discretized into 25 points, and the number of target points was chosen accordingly with respect to the photon flux Φ.

Unfortunately, due to issues during operation, there is no available data from the mission that would resemble the ideal case scenario. However, to at least give an idea of how the real optics used in the mission should behave, a set of tests was done before launch under laboratory conditions, where the optics were tested at different levels of photon flux, illustrated in figure 5.1. Although I was not able to find the specific conditions these tests were performed under, they should give an overall idea of how the general output of the lobster-eye optics used in the mission should look like.

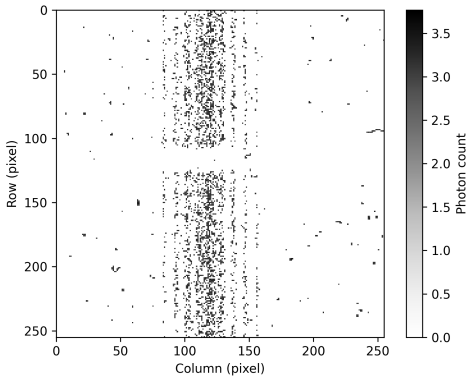

(a) Testing image one.

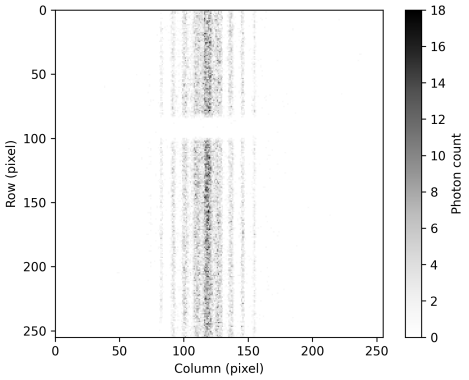

(b) Testing image two.

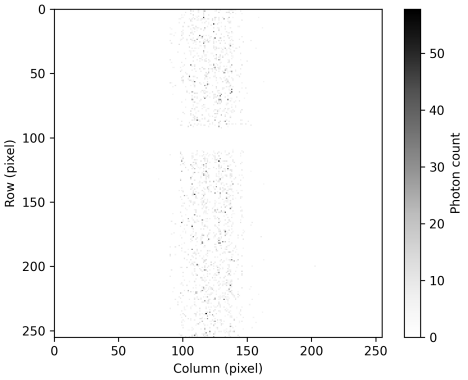

(c) Testing image three.

Figure 5.1: Images obtained during laboratory testing of the optics used in the VZLUSAT-1 mission. The conditions under which these images were obtained were unknown to me at the time of writing this thesis. The images serve to give an idea of the real behavior of the optics used in the mission. The position of the source can be determined from the shadow produced by the tungsten bar. Courtesy of the VZLUSAT-1 team.

5.2.1 Varying photon flux testing

First, the simulation was performed on three increasing levels of photon flux to illustrate how much information can be gathered at different levels of radiation, as seen in figure 5.2. At low radiation intensity, the shadow produced by the tungsten bar can be barely visible, and not much else can be determined, as seen in figure 5.2a.

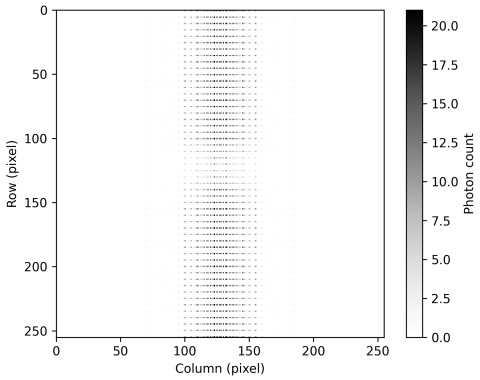

(a) Low photon flux. $\phi = 334.007\ \frac{\text{photons}}{\text{mm}^2 \cdot \text{s}}$.

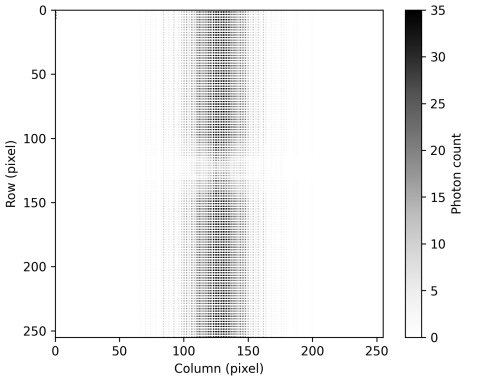

(b) Medium photon flux. $\phi = 2118.06\ \frac{\text{photons}}{\text{mm}^2 \cdot \text{s}}$

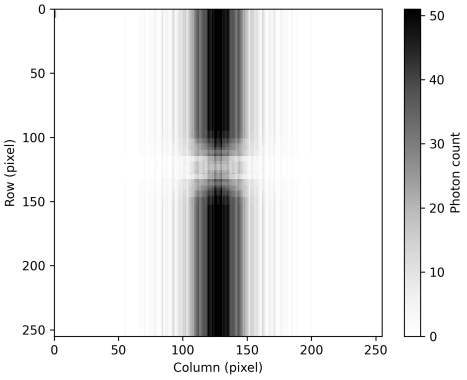

(c) High photon flux. $\phi = 8365.59\ \frac{\text{photons}}{\text{mm}^2 \cdot \text{s}}$

Figure 5.2: Results of simulations done at varying levels of photon flux ϕ. The exposure time considered was one second, and the source was aligned with the optics and the detector. The position of the source, which can be determined by the shadow produced by the tungsten bar placed in front of the optics, seems to depend on the level of the photon flux. The greater the intensity of radiation, the clearer the information gathered by the optics.

At a higher radiation intensity, the position along the vertical axis is much more apparent thanks to the shadow of the tungsten bar, and the position along the horizontal axis is much more defined, as seen in figure 5.2b. At high intensity, the characteristics of the image are much more defined, and the areas of maximum and minimum intensity along the vertical axis are more condensed into peaks, as seen in figure 5.2c.

5.2.2 Efficiency of focusing testing

In figure 5.3, the image is deconstructed into an image produced by rays directly passing through the optics without any interaction and an image produced only by rays reflected by the optics. This decomposition could prove useful in designing optics as the number of rays focused by the telescope should be as high as possible.

In the case illustrated in figure 5.3, the direct rays colliding with the detector accounted for approximately 3% of the total number of cast rays, and the reflected rays colliding with the detector accounted for approximately 4.2% of the total number of cast rays.

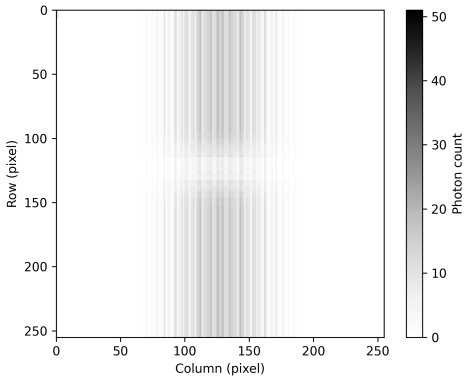

(a) Direct rays. $\phi = 8365.59\ \frac{\text{photons}}{\text{mm}^2 \cdot \text{s}}$

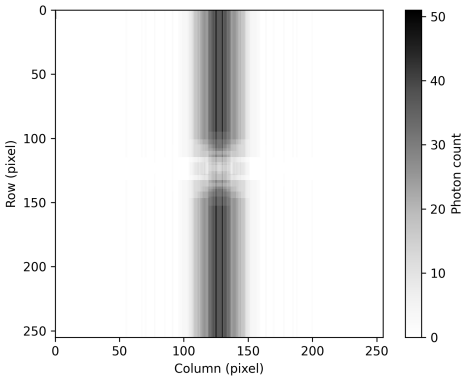

(b) Reflected rays. $\phi = 8365.59\ \frac{\text{photons}}{\text{mm}^2 \cdot \text{s}}$

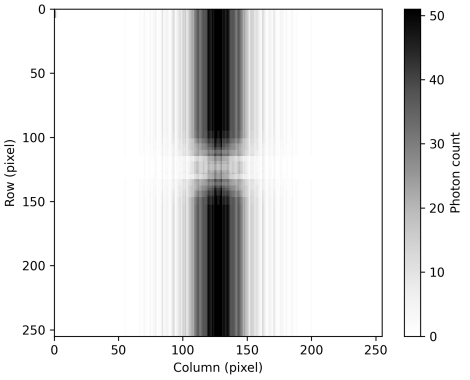

(c) All rays combined. $\phi = 8365.59\ \frac{\text{photons}}{\text{mm}^2 \cdot \text{s}}$

Figure 5.3: The result of the simulation of high photon flux $\phi = 8365.59\ \frac{\text{photons}}{\text{mm}^2 \cdot \text{s}}$ with time exposure of one second and the source aligned with the optics and the detector. The image is decomposed into direct and reflected rays to assess the efficiency of the optics. Ideally, the optics should reflect as many rays as possible.

5.2.3 Source position testing

Lastly, a set of simulations was performed to illustrate how the image changes depending on the source's position relative to the telescope. As seen in figure 5.4 the optics focus the rays

in the horizontal direction well as was designed. The source's position can be easily determined within the telescope's FOV.

Since the optics are designed to focus in one dimension only, the purpose of the tungsten bar comes into play when the source shifts in the vertical direction. This behavior can be seen in figure 5.5, where the source, together with the tungsten bar, produces a shadow in the image when the source shifts in the vertical direction thanks to which enables the viewer to estimate the source's position quite well. However, as can be seen in figure 5.2, this approach's efficiency depends on the source's radiation intensity.

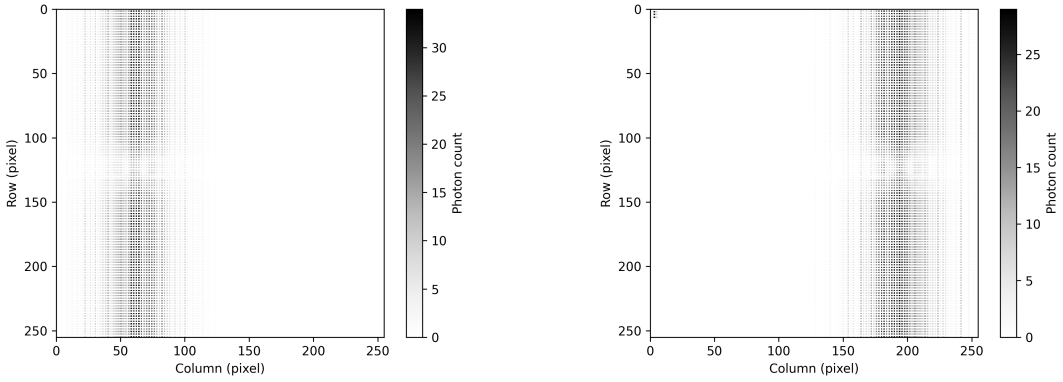

(a) Horizontal shift of $-0.75°$.

(b) Horizontal shift of $0.75°$.

Figure 5.4: Results of the simulations done at medium photon flux $\phi = 2118.06\,\frac{\text{photons}}{\text{mm}^2\cdot\text{s}}$ with the source shifted horizontally by $0.75°$ in both directions. The position of the source can be easily decoded if the distance of the source is known.

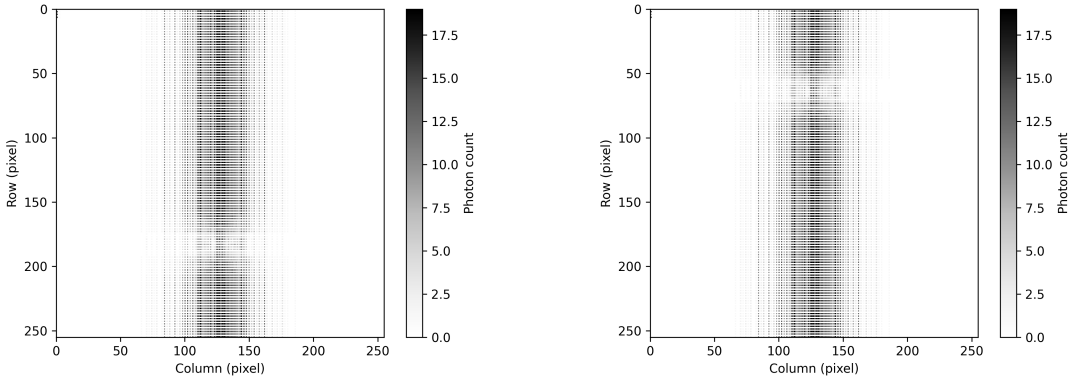

(a) Vertical $-0.75°$.

(b) Vertical $0.75°$.

Figure 5.5: Results of the simulation done at medium photon flux $\phi = 2118.06\,\frac{\text{photons}}{\text{mm}^2\cdot\text{s}}$ with the source shifted vertically by $0.75°$ in both directions. The position of the source can be easily decoded if the distance of the source is known.

5.3 Identification of potential flaws

From the data gathered from the telescope, it can be observed that due to the absence of shielding, under some conditions, the detector was exposed to radiation originating from outside the optics. This poses a significant problem since the detector being exposed to any stray radiation not filtered by the optics could damage it. Some of the shapes of radiation exposure seen in figure 5.6 may seem strangely similar to the curvatures of some openings present in the telescope's structure, which could let light through in some cases. A series of tests were performed to test this hypothesis, where the origin was positioned at an angle where light could potentially hit the detector without passing through the optics.

For this series of tests, the Sun was considered the source and modeled the same way as in the previous section 5.2. This time the rays did not pass through the optics; as a result, the target points were placed only on the detector's area.

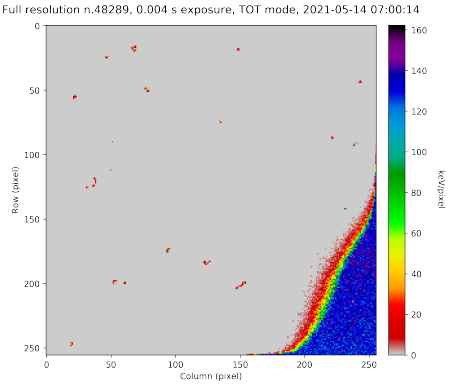

(a) Lower right corner illuminated.

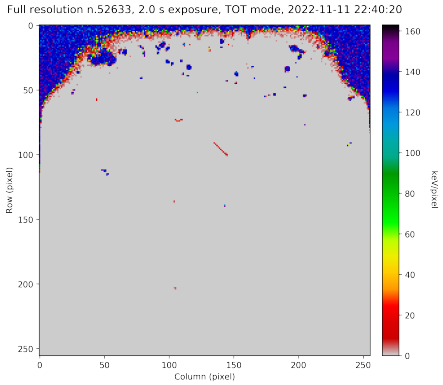

(b) Upper corners illuminated.

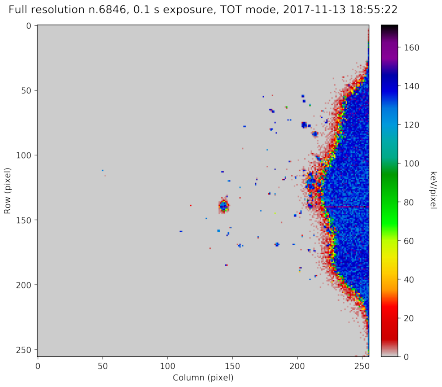

(c) Right side illuminated in a circular shape.

Figure 5.6: Real data gathered during the operation of the VZLUSAT-1 telescope, where the detector is illuminated in areas resembling the structure of the telescope. This implies that the telescope lets some rays pass to the detector without passing through the optics, which could pose an issue. Courtesy of the VZLUSAT-1 team.

5.3.1 Circular openings in the telescope's structure

The first candidate for the structural flaw that could have let light through is the circular opening above the optics module. As shown in figure 5.7, if the source is at an appropriate angle, it lets rays pass through the telescope and hit the detector.

The area possibly illuminated by rays passing through the circular opening above the optics can be seen in figure 5.7b. While the helix-like part of the telescope blocks some rays, the number of rays that reach the detector is significant. Additionally, the detector is designed primarily for X-ray radiation. In cases of different radiation, the photons can seep through the detector and obstruct the whole image and, in some cases, even damage it.

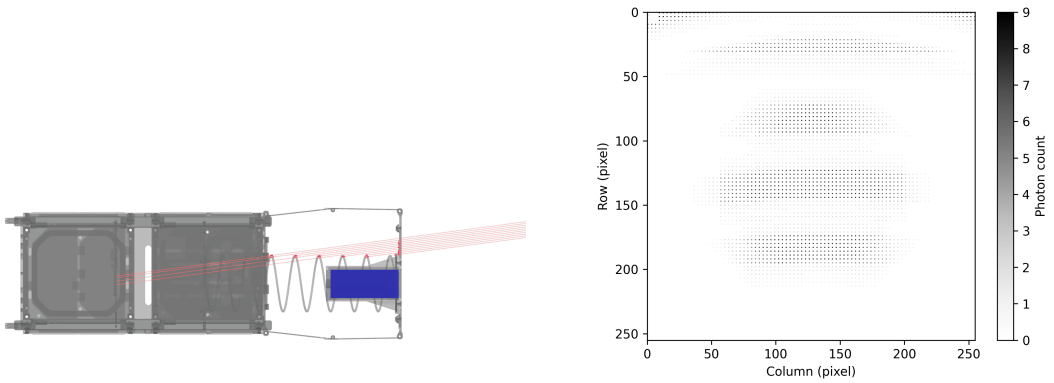

(a) Model view.

(b) Simulation output.

Figure 5.7: Model side view of the VZLUSAT-1 telescope when investigating the structural flaw of the upper circular opening done in Blender 5.7a. The resulting image of the investigation of the structural flaw 5.7b. The rays can clearly pass through the opening and take up a large area of the detector, which makes data gathering using the optics, in this case, impossible.

Similarly to the circular opening above the optics, the same behavior can be observed for the circular opening below the optics, as seen in figure 5.8. Since the opening below the optics is larger than the opening above, the area that can be illuminated also increases, and this time it covers almost the entire detector, as seen in figure 5.8b.

5.3.2 Side testing

Since there is a sizable unshielded gap between the optics and the detector, nothing prevents rays from hitting the detector from the sides of the telescope. Figure 5.9 illustrates a case where that happens. In the case shown in figure 5.9b, half the detector can be exposed to unfiltered radiation, which prevents valuable data gathering on a significant area of the detector.

.

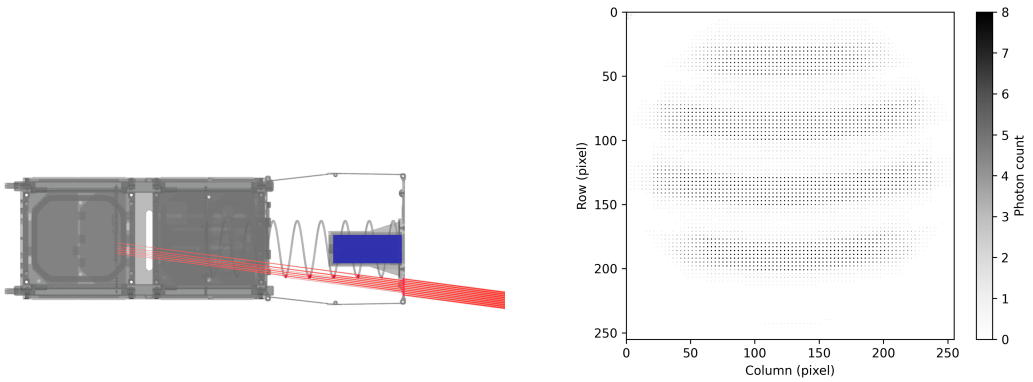

(a) Model view. (b) Simulation output.

Figure 5.8: Model side view of the VZLUSAT-1 telescope when investigating the structural flaw of the downward circular opening done in Blender 5.8a. The resulting image of the investigation of the structural flaw 5.8b. The rays can clearly pass through the opening and take up a large area of the detector, which makes data gathering using the optics, in this case, impossible.

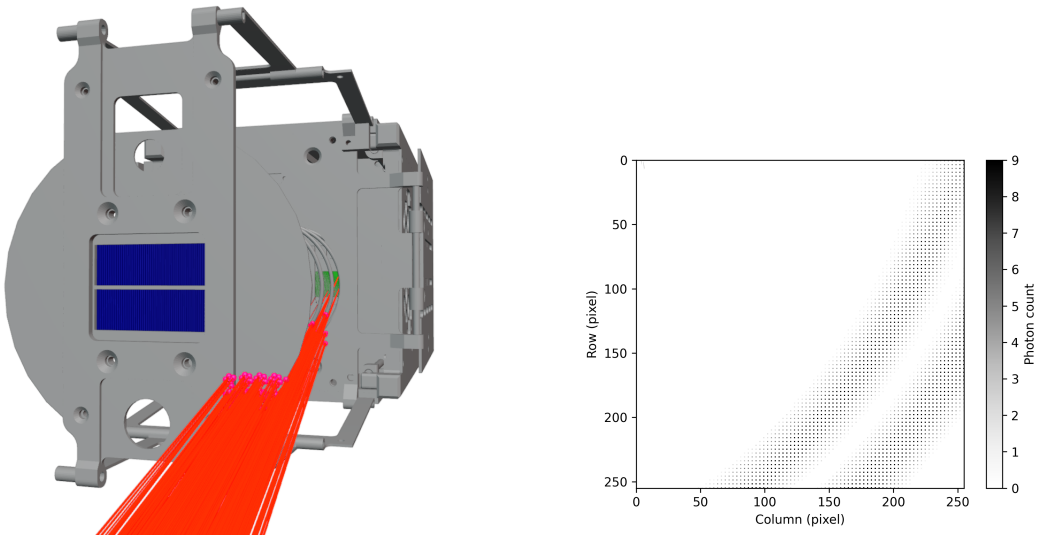

(a) Side isometric view. (b) Simulation output.

Figure 5.9: Model isometric view of the structural flaw investigation 5.9a. The telescope's structure is colored grey, the rays are colored red, the optics are colored blue, and the detector is colored green. The output of this simulation is depicted in 5.9b.

Chapter 6

REX Mission Testing

In contrast to the telescope used in the VZLUSAT-1 mission, the telescope employed in the REX mission incorporated radiation shielding to safeguard the detector from any stray radiation not captured by the optics. Consequently, testing for structural flaws becomes unnecessary.

However, a challenge encountered during the REX mission was the insufficient photon flux emitted by the observed source in the desired energy range. This lack of radiation hindered the mission, making it difficult to achieve meaningful results for optics testing. According to research done by the University of Birmingham [31], the energy flux of the Vela pulsar is approximately $9.4 \times 10^{-11}\,\mathrm{erg\,cm^{-2}\,s^{-1}}$ in the energy range of 4 to 25 keV. Even in the best-case scenario, where the energy of all the photons is only 4 keV, the resulting number of photons that would fall on the aperture of the optics during the exposure time of 282.5 seconds would be roughly 112 photons, which is still far too little for the optics to focus into a meaningful picture as can be seen in figure 6.1 which corresponds to the resulting image gathered during the mission. The radiation coming from the Vela Pulsar can't be discerned from background radiation and parasitic elements.

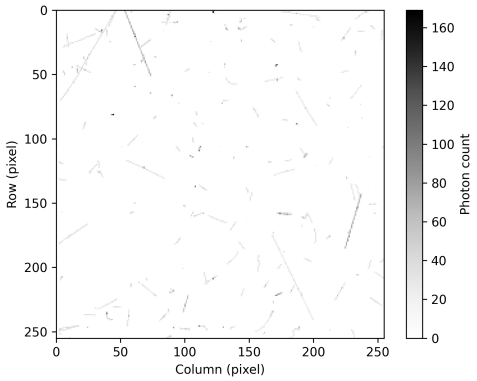

Figure 6.1: Real data gathered during the REX mission. As can be seen, the intensity of radiation of the Vela pulsar is not high enough for the pulsar to be identified. The image consists mostly of background radiation. Courtesy of the REX team.

The following simulations focus solely on what the resulting images would have looked like under favorable conditions.

6.1 Simulation setup

The focus of observation in the REX mission was the Vela SNR. Given the complex nature of the SNR, the simulations concentrated only on the Vela pulsar located at its center, which is the primary source of X-rays. Similar to the previous chapter's analysis of the Sun, the pulsar was discretized for the simulation in the same fashion, given its almost spherical shape. The approximate distance from LEO used in the simulation was equal to 9.461×10^{15} km, and the diameter was approximated to be 20 km. The parameters of the optics are summarized in 6.1.

Foil width	75.0 mm
Foil length	150.0 mm
Foil thickness	0.35 mm
Number of foils for each module	47
Front optics focal length	1345.0 mm
Rear optics focal length	1079.0 mm
Front optics FOV	1.05°
Rear optics FOV	1.3°
Aperture area	676 mm^2

Table 6.1: Parameters of the 2D schmidth type lobster-eye optics.

6.2 Ideal case scenario

For the ideal case scenario, the pulsar was discretized as previously described into 25 points, and three simulations with different photon flux levels were performed. The number of target points was set accordingly to reflect the time exposure of 282.5 seconds corresponding to the time exposure of the real telescope.

6.2.1 Varying photon flux testing

To test the optics under favorable conditions, three simulations were performed with increasing levels of photon flux. At a lower intensity, as seen in figure 6.2a, most of the rays that hit the detector are untouched by the optics, and while an area of higher intensity can be made out, it could still be overshadowed by background radiation.

As the intensity increases, as seen in figure 6.2b, the typical cross pattern generated by the reflected rays in the 2D lobster-eye optics can be observed, which makes the identification of the source's position possible. At high intensity, as seen in figure 6.2c, the cross pattern is even clearer, and the geometrical arrangement of the source is more apparent in the center.

6.2.2 Efficiency of focus testing

The high-intensity image is deconstructed in the same fashion as in the VZLUSAT-1 simulation 5.2.2. In the case of 2D lobster-eye optics, the focusing ability is much better than the one-dimensional counterpart. In this case, the direct rays make up approximately 1.8% of the number of rays cast on the aperture, while reflected rays make up 4.6% of the number of rays cast on the aperture. As can be seen in figure 6.3, the direct rays serve in the final picture only as background, while most of the information about the source is encapsulated by the reflected rays.

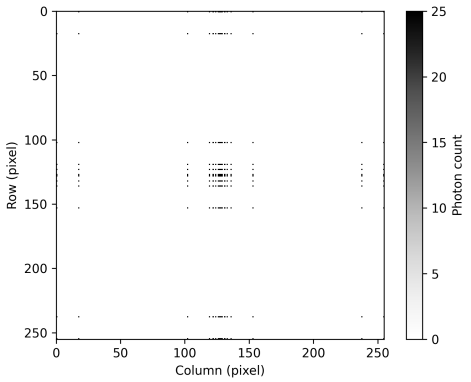

(a) Low photon flux. $\phi = 0.411 \frac{\text{photons}}{\text{mm}^2 \cdot \text{s}}$

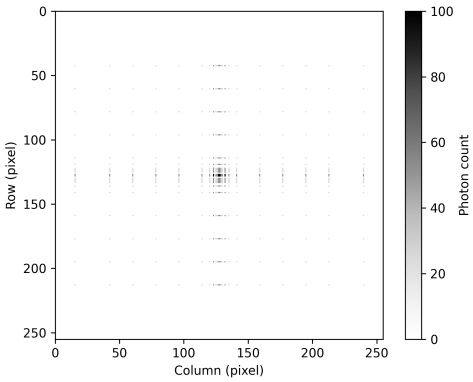

(b) Higher photon flux. $\phi = 1.471 \frac{\text{photons}}{\text{mm}^2 \cdot \text{s}}$

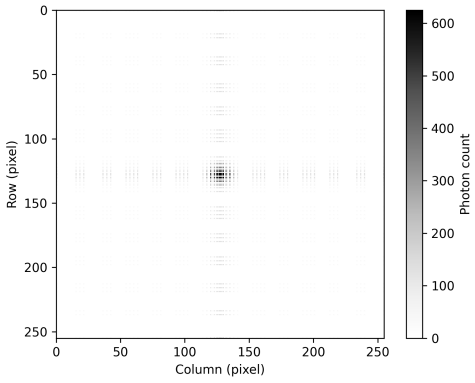

(c) High photon flux. $\phi = 13.072 \frac{\text{photons}}{\text{mm}^2 \cdot \text{s}}$

Figure 6.2: Results of simulations done at varying levels of photon flux ϕ. The exposure time considered was 282.5 s, which corresponds to the exposure time of the real REX telescope, and the source was aligned with the optics and the detector to form an image at the center.

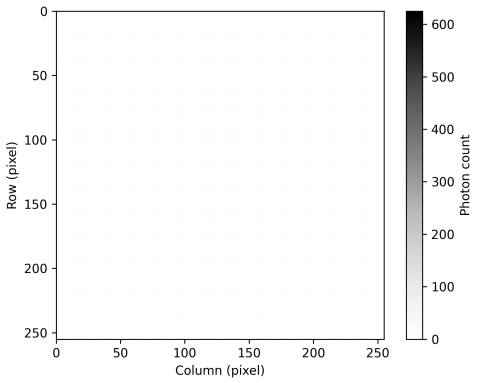

(a) Direct rays. $\phi = 13.072\ \frac{\text{photons}}{\text{mm}^2 \cdot \text{s}}$

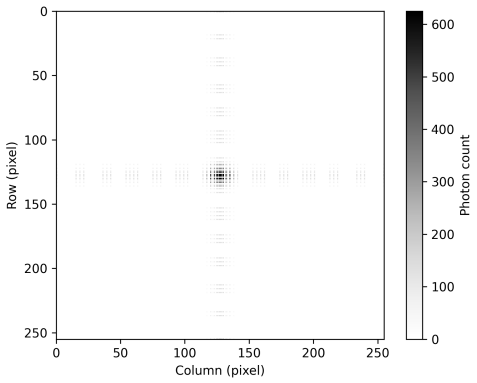

(b) Reflected rays. $\phi = 13.072\ \frac{\text{photons}}{\text{mm}^2 \cdot \text{s}}$

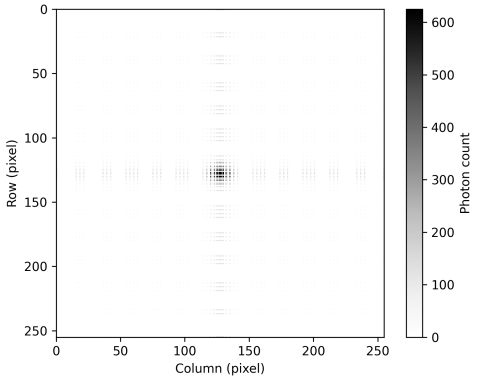

(c) Direct and reflected rays combined.
$\phi = 13.072\ \frac{\text{photons}}{\text{mm}^2 \cdot \text{s}}$

Figure 6.3: The result of the simulation of high photon flux $\phi = 13.072\ \frac{\text{photons}}{\text{mm}^2 \cdot \text{s}}$ with time exposure 282.5 s, which corresponds to the exposure time of the real REX telescope, and the source aligned with the optics and the detector to form an image at the center. The image is decomposed into direct and reflected rays to assess the efficiency of the optics. The final image is comprised mainly of the reflected rays, which is the intended behavior of the optics.

6.2.3 Source position testing

While the sounding rocket should, under ideal circumstances, be aimed at the source directly, a slight deviation within the optics FOV is possible. To test how the output would change in this scenario, the simulator could be useful. To test a possible scenario, a simulation where the source deviates from the center of the optics by 0.1 deg in both axes was performed. As can be seen in figure 6.4, even at lower levels of photon flux, the cross pattern is retained; however, a significant amount of rays are blocked by the optics.

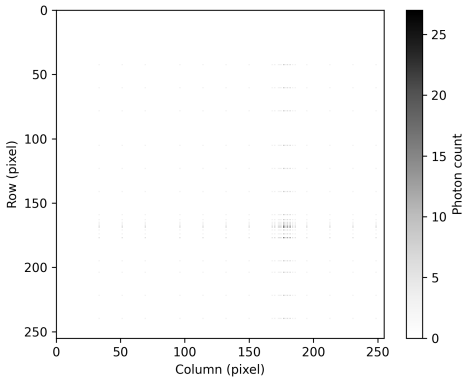

Figure 6.4: Resulting image of the simulation done at medium photon flux $\phi = 1.471 \frac{\text{photons}}{\text{mm}^2 \cdot \text{s}}$ with the source shifted by 0.1 deg in both directions. The clarity of the image is significantly hindered when the source is shifted. The importance of the sounding rocket maintaining the telescope aimed directly at the source is apparent.

Chapter 7

Conclusion

This thesis presented the challenges associated with developing optics for space telescopes, focusing specifically on lobster-eye optics. To improve our understanding of how lobster-eye optics behave under different circumstances, a ray-tracing simulator with the unique properties of lobster-eye optics in mind was developed and subsequently tested on various scenarios inspired by real-life missions VZLUSAT-1 and REX.

The missions examined in this work, although different in nature, shared common challenges related to weight, shielding, and cost. By simulating the ideal behavior of the telescopes used in these missions, the impact of design choices made by the developers was assessed. Furthermore, a series of tests were conducted to identify and understand the flaws that hindered the missions. A thorough analysis was performed, revealing potential flaws and providing insights into the operational behavior of the telescopes under different conditions.

The findings of this work demonstrated that the reduction of shielding to save on weight and cost could have significant drawbacks for the testing of lobster-eye optics. It was demonstrated that the efficiency of lobster-eye optics is highly dependent on the intensity of radiation emitted by the observed objects. Thus, future missions should ensure access to reliable information regarding the source's radiation spectrum. Fortunately, the deployment of more telescopes focused on high-energy radiation in recent years has facilitated this process.

Moving forward, there are several improvements that could enhance the performance of the simulator, namely computational efficiency. A possible improvement could be brought about by implementing a bounding volume hierarchy to the ray tracing, commonly used in other ray tracing algorithms. Additionally, optimizing the simulator for GPUs could leverage the processing power of modern graphics cards and greatly improve the simulator's speed. While the use of Blender to visualize the simulations provides many useful tools for manipulating the scene, a major drawback is the restricted number of objects that Blender can visualize at once. For the purpose of visualizing more complex cases, a different tool needs to be developed.

In conclusion, the work presented provides a good basis for further improvements to X-ray tracing simulators. As the simulator is utilized by dedicated researchers in the field of X-ray astronomy, hopefully, more features will be added to the simulator to more accurately portray the complex behavior of these optics. The simulator should both facilitate the development of new designs and prevent similar issues encountered during the missions discussed in the future.

Chapter 8

References

[1] D. Farrah, K. Croker, M. Zevin, *et al.*, "Observational Evidence for Cosmological Coupling of Black Holes and its Implications for an Astrophysical Source of Dark Energy," *The Astrophysical Journal Letters*, vol. 944, no. 2, p. L31, Feb. 2023.

[2] M. Urban, O. Nentvich, T. Báča, *et al.*, "REX: X-ray experiment on the water recovery rocket," *Acta Astronautica*, vol. 184, pp. 1–10, 2021.

[3] D Masutti, A Denis, R Wicks, *et al.*, "The QB50 mission for the investigation of the mid-lower thermosphere: Preliminary results and lessons learned," in *Proc. 15th Int. Planetary Probe Workshop*, 2018.

[4] H. M. Günther, J. Frost, and A. Theriault-Shay, "MARXS: A Modular Software to Ray-trace X-Ray Instrumentation," *The Astronomical Journal*, vol. 154, no. 6, p. 243, Nov. 2017.

[5] D. M. Miles, R. L. McEntaffer, T. B. Schultz, *et al.*, "An introduction to the water recovery x-ray rocket," in *UV, X-Ray, and Gamma-Ray Space Instrumentation for Astronomy XX*, SPIE, vol. 10397, 2017, pp. 205–212.

[6] NASA, *Proposed NASA Mission Employs 'Lobster-Eye' Optics to Locate Source of Cosmic Ripples*, `https://www.nasa.gov/feature/goddard/2017/proposed-nasa-mission-employs-lobster-eye-optics-to-locate-source-of-cosmic-ripples`, Accessed: 05-05-2023, 2017.

[7] NASA Science, *Vela Pulsar*, https://www.nasa.gov/mission$_p$*ages/chandra/multimedia/vela*2012.*html*, Accessed: 05-05-2023, 2017.

[8] A.-C. Probst, T. Döhring, M. Stollenwerk, M. Wen, and L. Proserpio, "Iridium coatings for space based x-ray optics," in *International Conference on Space Optics — ICSO 2016*, B. Cugny, N. Karafolas, and Z. Sodnik, Eds., International Society for Optics and Photonics, vol. 10562, SPIE, 2017, 105621E.

[9] M. Urban, O. Nentvich, V. Stehlikova, T. Baca, V. Daniel, and R. Hudec, "VZLUSAT-1: Nanosatellite with miniature lobster eye X-ray telescope and qualification of the radiation shielding composite for space application," *Acta Astronautica*, vol. 140, pp. 96–104, 2017.

[10] D. Zhao, C. Zhang, W. Yuan, S. Zhang, R. Willingale, and Z. Ling, "Geant4 simulations of a wide-angle x-ray focusing telescope," *Experimental Astronomy*, vol. 43, pp. 267–283, 2017.

[11] T. Baca, M. Platkevic, J. Jakubek, *et al.*, "Miniaturized X-ray telescope for VZLUSAT-1 nanosatellite with Timepix detector," *Journal of Instrumentation*, vol. 11, no. 10, p. C10007, 2016.

[12] E. of Encyclopaedia Britannica, *Cassegrain reflector*, `https://www.britannica.com/science/Cassegrain-reflector`, Accessed: 05-05-2023, 2016.

[13] V. Tichý, R. Hudec, and Š. Němcová, "Effective algorithm for ray-tracing simulations of lobster eye and similar reflective optical systems," *Experimental Astronomy*, vol. 41, pp. 377–392, 2016.

[14] M Platkevic, "Signal processing and data read-out from position sensitive pixel detectors," Ph.D. dissertation, Ph. D. Thesis, Czech Technical University in Prague, 2014.

[15] P. A. Lightsey, C. B. Atkinson, M. C. Clampin, and L. D. Feinberg, "James Webb Space Telescope: large deployable cryogenic telescope in space," *Optical Engineering*, vol. 51, no. 1, p. 011 003, 2012.

[16] E. Buis and G. Vacanti, "X-ray tracing using Geant4," *Nuclear Instruments and Methods in Physics Research Section A: Accelerators, Spectrometers, Detectors and Associated Equipment*, vol. 599, no. 2, pp. 260–263, 2009.

[17] S Krucker, M Battaglia, P. Cargill, *et al.*, "Hard X-ray emission from the solar corona," *The Astronomy and Astrophysics Review*, vol. 16, pp. 155–208, 2008.

[18] B. Lehmer, W. Brandt, D. Alexander, *et al.*, "Tracing the Mass-Dependent Star Formation History of Late-Type Galaxies Using X-Ray Emission: Results from the Chandra Deep Fields," *The Astrophysical Journal*, vol. 681, no. 2, Mar. 2008.

[19] W. J. Smith, *Modern optical engineering: the design of optical systems*. McGraw-Hill Education, 2008.

[20] I. Sujová, R. Hudec, and F. Munz, "Lobster Eye X-ray Monitor and Blazars," Jan. 2008.

[21] X. Llopart, R. Ballabriga, M. Campbell, L. Tlustos, and W. Wong, "Timepix, a 65k programmable pixel readout chip for arrival time, energy and/or photon counting measurements," *Nuclear Instruments and Methods in Physics Research Section A: Accelerators, Spectrometers, Detectors and Associated Equipment*, vol. 581, no. 1, pp. 485–494, 2007, VCI 2007.

[22] R. Pogge, *Astronomy 161: An Introduction to Solar System Astronomy*, `https://www.astronomy.ohio-state.edu/pogge.1/Ast161/Au06/Unit4/telescopes.html`, Accessed: 05-05-2023, 2006.

[23] T. Möller and B. Trumbore, "Fast, minimum storage ray/triangle intersection," in *ACM SIGGRAPH 2005 Courses*, 2005, 7–es.

[24] G. K. Skinner, P. von Ballmoos, N. Gehrels, and J. Krizmanic, "Fresnel lenses for x-ray and gamma-ray astronomy," in *Optics for EUV, X-Ray, and Gamma-Ray Astronomy*, SPIE, vol. 5168, 2004, pp. 459–470.

[25] S. Agostinelli, J. Allison, K. Amako, *et al.*, "Geant4—a simulation toolkit," *Nuclear Instruments and Methods in Physics Research Section A: Accelerators, Spectrometers, Detectors and Associated Equipment*, vol. 506, no. 3, pp. 250–303, 2003.

[26] P. J. E. Peebles and B. Ratra, "The cosmological constant and dark energy," *Rev. Mod. Phys.*, vol. 75, pp. 559–606, 2 Apr. 2003.

[27] F. Weber, "Nuclear and High-Energy Astrophysics," in *Hadron Physics 2002: Topics on the Structure and Interaction of Hadronic Systems*, World Scientific, Aug. 2003, pp. 73–134.

[28] A. N. Cha, K. R. Sembach, and A. C. Danks, "The Distance to the Vela Supernova Remnant," *The Astrophysical Journal*, vol. 515, no. 1, p. L25, Feb. 1999.

[29] C. Simpson and P. Eisenhardt, "The Detection and Photometric Redshift Determination of Distant Galaxies Using SIRTF's Infrared Array Camera," *Publications of the Astronomical Society of the Pacific*, vol. 111, no. 760, p. 691, Jun. 1999.

[30] A. G. Riess, A. V. Filippenko, P. Challis, *et al.*, "Observational Evidence from Supernovae for an Accelerating Universe and a Cosmological Constant," *The Astronomical Journal*, vol. 116, no. 3, p. 1009, Sep. 1998.

[31] A. Willmore, C. Eyles, G. Skinner, and M. Watt, "Hard X-ray emission from the Vela supernova remnant," *Monthly Notices of the Royal Astronomical Society*, vol. 254, no. 1, pp. 139–145, 1992.

[32] W. Heitler, *The quantum theory of radiation*. Courier Corporation, 1984.

[33] J. R. P. Angel, "Lobster Eyes As X-Ray Telescopes," in *Space Optics Imaging X-Ray Optics Workshop*, M. C. Weisskopf, Ed., International Society for Optics and Photonics, vol. 0184, SPIE, 1979, pp. 84 –85.

[34] L. Williams, "Casting curved shadows on curved surfaces," in *Proceedings of the 5th annual conference on Computer graphics and interactive techniques*, 1978, pp. 270–274.

[35] W. Schmidt, "A proposed X-ray focusing device with wide field of view for use in X-ray astronomy," *Nuclear Instruments and Methods*, vol. 127, no. 2, pp. 285–292, 1975.

[36] A. Einstein, "On a Heuristic Point of View about the Creation and Conversion of Light," *The Old Quantum Theory*, pp. 91–92, Dec. 1967.

[37] A. H. Compton, "A quantum theory of the scattering of X-rays by light elements," *Physical review*, vol. 21, no. 5, p. 483, 1923.

[38] J. W. S. B. Rayleigh, *On the scattering of light by small particles*. 1871.

[39] *Virtual Pinhole Camera Model*, https://www.scratchapixel.com/lessons/3d-basic-rendering/3d-viewing-pinhole-camera/virtual-pinhole-camera-model.html, Accessed: 05-05-2023.

Chapter A

Appendix A

This appendix serves to give a brief overview of the source code contained in the CD that this thesis is shipped with. All the files contained in the CD and their descriptions are summarized in table A.1.

File Name	Description
src/geometry.py	This file contains the tools for the geometry used in the simulator.
src/Results.py	This file defines how the results should be formatted in the pickle file.
blender_api_plot.py	This file contains the script that is used for visualization in Blender.
collision_check.py	This file contains an example case of how collisions with an STL model are handled.
rex_raytracing.py	This file contains the script that was used for REX simulations.
vzlu_raytracing.py	This file contains the script that was used for VZLUSAT-1 simulations.
REX_transformed.stl	This is the STL model of the REX telescope.
VZLUSAT_transformed.stl	This is the STL model of the VZLUSAT-1 telescope.

Table A.1: Content of the CD.